Velocity field analysis in an experimental cavitating mixing layer

Vincent Aeschlimann, Stéphane Barre, Henda Djeridi

Velocity field analysis in an experimental cavitating mixing layer

Vincent Aeschlimann, Stéphane Barre, and Henda Djeridi

Citation: Phys. Fluids **23**, 055105 (2011); doi: 10.1063/1.3592327
View online: http://dx.doi.org/10.1063/1.3592327
View Table of Contents: http://pof.aip.org/resource/1/PHFLE6/v23/i5
Published by the American Institute of Physics.

Velocity field analysis in an experimental cavitating mixing layer

Vincent Aeschlimann,[1,a)] Stéphane Barre,[1] and Henda Djeridi[2]
[1]*LEGI, Grenoble-INP, UMR 5519, BP 53, 38 041 Grenoble Cedex 9, France*
[2]*Université Européenne de Bretagne, Laboratoire de Physique des Océans, UMR 6523, 6 Avenue le Gorgeu, BP 809, 29 285 Brest Cedex, France*

(Received 20 October 2010; accepted 19 April 2011; published online 27 May 2011)

The purpose of this experimental study was to analyze a two-dimensional cavitating shear layer. The global aim of this work was to improve understanding and modeling of cavitation phenomena, from a 2D turbulent shear flow to rocket engine turbopomp inducers. This 2D mixing layer flow provided us with a well documented test case to be used for comparisons between behavior with and without cavitation. Similarities and differences enabled us to characterize the effects of cavitation on flow dynamics. The experimental facility enabled us to set up a mixing layer configuration with different cavitation levels. The development of a velocity gradient was observed inside a liquid water flow using PIV–LIF (particle image velocimetry–laser induced fluorescence). Kelvin-Helmholtz instabilities developed at the interface and vaporizations and implosions of cavitating structures inside the vortices were observed. The mixing area grew linearly, showing a constant growth rate, for the range of cavitation levels studied. The spatial development of the mixing area seemed hardly to be affected by cavitation. Particularly, the self-similar behavior of the mean flow was preserved despite the presence of the vapor phase. Successive vaporizations and condensations of the fluid particles inside the turbulent area generated additional velocity fluctuations due to the strong density changes. Moreover, when cavitation developed, the Kelvin-Helmholtz vortex shape was modified, inducing a strong anisotropy (vortex distortion as ellipsoidal form) due to the vapor phase. The main results of this study clearly showed that the turbulence-cavitation relationship inside a mixing layer was not simply a change of compressibility properties of the fluid in the turbulent field, but a mutual interaction between large and small scales of the flow due to the presence of a two-phase flow.
 [doi:10.1063/1.3592327]

I. INTRODUCTION

A. Background

This work follows previous experimental and numerical studies carried out by the Turbomachinery and Cavitation team (now called Energétique team) of LEGI (Grenoble, France). The purpose was to improve understanding and modeling of cavitation phenomena in the turbulent complex flows. The studies were led in collaboration with the French Space Agency (CNES) and the rocket engine division of Snecma. The global aim was to analyze free sheared cavitating flows in rocket engine turbopomp inducers, where the run fluids are cryogenic fluids, liquid hydrogen (LH_2), and liquid oxygen (LOx). In this context, experimental and numerical studies have been performed in the laboratory with cold water and refrigerant R114 on Venturi geometries.[1] These previous studies have provided a good understanding of the dynamic behavior of an attached cavitating sheet on the wall. The oscillating frequency of the vapor sheet has been analyzed; the "break-off cycle" has been characterized. Velocity measurements highlighted the re-entrant jet dynamic. Several phenomena were suspected to influence the cavitation development: wall effect, flow separation, shear stress, turbulence ratio, water quality… The complexity of the flow prevented us from telling apart the influence of each parameter on cavitation production. This conclusion led us to carry out the experimental study of a more fundamental case: a two-dimensional mixing layer. This particular type of flow has been mainly chosen because of the high number of results present in the literature. It can be noticed that cavitating sheared flows are also found in a wide variety of propulsion and power systems like pumps, valves, nozzles, injectors, marine propellers, hydrofoils as abstracted in Knapp *et al.*[2] Actually, all separated cavitating flow regions involve a turbulent free shear layer as shown in Katz,[3] Wang *et al.*,[4] Katz *et al.*,[5] Wang *et al.*[6] Cavitating free shear flows are also found in the wake of bluff bodies as illustrated by Kermeen *et al.*,[7] Young *et al.*,[8] and Belahadji *et al.*[9]

However, its interest in the context of the present study goes well beyond its status of academic basic benchmark flow type. When dealing with cavitation on spatial turbopump inducers, one may find two major cavitation schemes. The first one consists in attached cavitation sheets on the suction side of the inducer blades. The second main cavitation sketch consists in sheared cavitation which occurs mainly in the peripherical area of the rotor close to the stator (tip clearance cavitation).

Concerning the attached cavitation (blade cavitation sheet) it consists mainly in a turbulent boundary layer which exhibits, at its rear part, a fluctuating detached zone called the "re-entrant jet." This zone is mainly characterized by a

a)Author to whom correspondence should be addressed. Electronic mail: Vincent.Aeschlimann@legi.grenoble-inp.fr

shedding process of detached large scale structures. A lot of literature is available about the re-entrant jet dynamics (see e.g., Refs. 1, 10–15). In fact, this zone is a cavitating turbulent shear layer between a negative velocity zone, close to the wall, and a positive velocity zone, at the outer part of the sheet. Most of the blade cavitation sheet dynamics is driven by this free shear layer behavior. Furthermore, as shown in Barre *et al.*[1] and Coutier *et al.*,[16] classically used URANS numerical simulations of such flows fail to reproduce accurately its dynamics. This fact justifies that a strong experimental effort has to be performed on a 2D cavitating mixing layer in order to obtain a well documented reference case to help both turbulence and cavitation models validations.

When dealing with the sheared cavitation found in the external part of the inducer blades (tip clearance cavitation), one may recognize that it has a strong importance for both the inducer's performance in cavitating regime and also on global cavitation related instabilities. Hassan *et al.*[17] have shown, by performing tomographic x-ray absorption measurements on a real inducer, that up to 40% of the total vapor volume contained in a cavitating inducer is localized in this tip clearance cavitation zone. This cavitation is due to the presence of both tip vortices and backflow structure which exists at the inducer inlet in some low flow rates regimes. A lot of work has been performed to describe both experimentally and numerically its dynamics (see e.g., Refs. 18–23). The backflow consists in a rotating annular free shear layer in which the diphasic content of the eddies may vary with respect to the inducer inlet cavitation number. The influences of the cavitating characteristics of the backflow are important in term of the inducer global performance. However, the strongest effect of the backflow lies in its influence on cavitation instabilities which are directly related to the vapor content into the backflow turbulent structures. The vapor quantity directly modifies the overall compressibility of the entire rocket engine feeding system leading to drastic changes in natural frequencies which are, at first order, driven by the cavitating behavior of the backflow. At the present time numerical simulations fail to reproduce accurately those instabilities. This leads to the necessity of improving both turbulence and cavitation modeling strategy. An accurate experimental study of the turbulent cavitating mixing layer may help this improvement.

Another reason to use the plane mixing layer as a test case is that the parameters characterizing the self-similarity properties of the flow are well known whether compressible or not, whether involving liquid or gas. These parameters are often based on inlet conditions and liquid properties.[24–26] However, a lack of knowledge remained concerning the behavior of two-phase flows and especially cavitating flows where no gas was present at the inlet.

The present study was carried out on a 2D shear layer test bed where no wall effect interfered with the flow. The objective was to obtain refined database and informations concerning the behavior of the liquid phase under different cavitation levels. This reference test has provided us a well documented test case to be used for numerical simulations of the complex turbulent two-phase flow and in order to quantify the turbulence-cavitation interactions.

Previous works have begun to analyze cavitating mixing layers; for example, 0'Hern[27] studied the cavitating mixing layer developing on a sharp-edged plate. These works focused on the inception of cavitation inside the mixing area with large physical dimensions allowing a detailed optical flow diagnostics. They put in evidence the importance of the streamwise vortices in the cavitation inception process as the key to explain the commonly observed Reynolds dependence of the inception index. More recently, Iyer *et al.*[28] studied the influence of developed cavitation on the flow of a turbulent shear layer using PIV–LIF techniques (particle image velocimetry–laser induced fluorescence). Their visual observations of the shear layer suggested that the overall formation, growth, and convection of the primary and secondary vortical structures are not significantly affected by the presence of the vapor phase and the largest differences between cavitation and non-cavitating case in the center of the shear layer consisted in the increase of turbulent fluctuations by about 15%. A DNS numerical simulation of this flow configuration was also performed. Although the simulation Reynolds number was lower than the experimental one, the obtained results showed a quite good qualitative agreement with experimental one. Particularly they found that the eddy viscosity is poorly affected by cavitation and that, at the opposite, cavitation has a strong effect on the Reynolds stress tensor anisotropy. Bubbles collapse increased the turbulence levels, as expected by Laberteaux *et al.*[29] Taking into account these results, one of the aims of the current research was to characterize the turbulent-cavitation relationship through refined measurements of the liquid phase and vapor phase dynamics using PIV–LIF techniques, X-ray attenuation detection,[30] and high resolution visualizations with specific signal processing concerning the determination of the turbulent length scales of the flow for higher void ratios (about 17% compared to 1.5% for the Iyer *et al.*[28] study). The results presented here focus on the statistical analysis of mean and turbulent velocity measurements to assess the turbulent kinetic energy, the anisotropy tensor, and characteristic length scales in order to highlight the physical mechanism of the turbulent agitation due to the vapor phase. It can be noticed that PIV–LIF has been more and more often used in multiphase flows and especially in cavitating ones. For example, Laberteaux *et al.*[29] used this technique to analyze the flow dynamics in the wake of an attached cavitation sheet where the Strouhal number and the Reynolds stress tensor where estimated. An interesting use of PIV–LIF was to couple it with a standard visualization camera.[31–33] By synchronizing the acquisition of the two apparatus, it became possible to simultaneously perform instantaneous velocity field measurements and cavitation structure visualization. Another original PIV technique adaptation for velocity measurement in a cavitating two-phase flow has been used by Vabre *et al.*,[34] where ultra-fast x-ray imaging was performed using absorbent particles. However, the spatial modification of the vortices due to cavitation was not clearly investigated. In this objective, we present here higher order moments of statistical analysis of the 2D velocity field using PIV–LIF techniques in the longitudinal section (X, Y). The self-similarity of the flow was characterized by the dimensionless

analysis of mean velocity profiles and fluctuation profiles. Parameters that characterized the flow dynamic were studied and quantified: vorticity thickness, growth rate, and Reynolds tensor components. Turbulent kinetic energy and the anisotropy tensor components were also analyzed and estimated. From the spatial correlation, transversal and longitudinal integral scales were estimated, providing an estimation of the two-phase structure size and turbulent diffusivity. The refined grid gave us access to the evolution of the turbulent viscosity inside the mixing area which was also observed for comparison with a classical numerical model used for cavitating flows.

B. Cavitating shear layer

A shear layer is characterized by a discontinuity between two flows. In the present study, the development of a velocity gradient was observed. The time-averaged velocity profiles are illustrated in Fig. 1. Kelvin-Helmholtz instabilities are developed at the interface and became eddies along the x-axis. The pressure was lower at the center of the eddies than in the external layers; this was where the liquid started to evaporate. To illustrate this, an example is given in Fig. 2, where an instantaneous picture of the cavitating shear layer is presented. Cavitating eddies in the shear layer (Kelvin-Helmholtz structures) are clearly identified and frozen by the 20 μs shutter time of the high speed camera (the vapor is white and liquid is dark). The incoming flows were cold liquid water and the vapors appearing inside the eddies in the mixing area are due to sheared cavitation.

The classical shear layer is defined by its growth rate δ' which remains constant along the x-axis when the flow is self-preserved,

$$\delta' = \frac{d\delta}{dx}, \tag{1}$$

where δ is a characteristic thickness of the mixing area. In this study we used δ_ω, the vorticity thickness defined as follows:

$$\delta_\omega = \frac{U_1 - U_2}{\left.\frac{dU}{dy}\right|_{\max}} = \frac{\Delta U}{\left.\frac{dU}{dy}\right|_{\max}}. \tag{2}$$

The main interest for studying such flows comes from the original configuration of two one-phase subsonic liquid flows creating a two-phase compressible zone in the mixing area only. Actually, the speed of sound in a two-phase mixture is

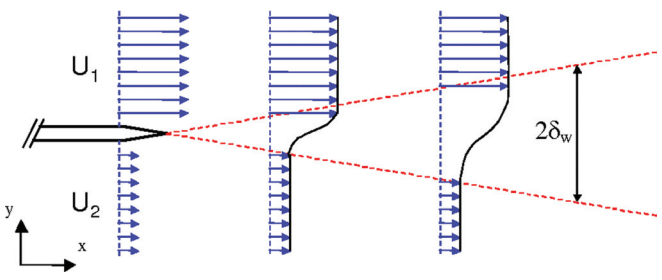

FIG. 1. (Color online) Averaged velocity profiles in the shear layer.

FIG. 2. Instantaneous picture of the cavitating shear layer (Weinberger SpeedCam Visario—shutter time 20 μs).

about a hundred or a thousand times smaller than in pure vapor or liquid, respectively.[35] In order to better understand the behavior of the cavitating turbulent structures, it was necessary to discriminate the compressibility effect and the vapor phase effects. For this reason, the present study attempts to compare the compressibility effect on one-phase supersonic mixing layers to that on this cavitating mixing layer.

Two different types of behavior occur, depending on the properties of the fluid. The first is incompressible; in this case, when ΔU increases, the growth rate also increases. At the opposite, in the compressible case, the scaling parameter is the convective Mach number, M_c, of the large eddies as defined in Papamoschou *et al.*[25]. When M_c increases, δ_ω' decreases. This phenomenon is called the net effect of compressibility. It can be quantified by the convective Mach number M_c which depends on the velocity difference and the speed of sound of each external flow,

$$M_c = \frac{U_1 - U_2}{(a_1 + a_2)}, \tag{3}$$

where a_1 and a_2 are the speed of sound for the two external flows.

In the present configuration, $a_1 = a_2 \approx 1500$ m/s in liquid water.

When M_c is lower than 0.5, the flow exhibits incompressible behavior.[24,25] In our case, the convective Mach number was 0.004: the flow can be considered incompressible. Thus, the cavitating shear layer is not expected to develop in the same way as the supersonic gas shear layer described in Brown *et al.*[24] because of the cavitation phenomenon.

Results will be used for numerical simulation validation where compressibility models are implemented in cavitating flows similarly to those used for supersonic gas flows.[16,31,32,36]

II. METHODS

A. Experimental setup

Experiments were conducted at CREMHyG, the hydraulic research center of Grenoble, on a shear layer test bed. The rectangular test section was 300 mm long and had a cross-section that expands from 80×80 mm at the inlet to 80×88.8 mm at the outlet. The studied shear layer was two-dimensional; the inlet section was divided in two. The splitting plate was 6 mm thick and ended with a rounded edge of 0.2 mm radius. Liquid water was used as the test fluid for this experiment.

The test bed was set in a closed hydraulic circuit that included a regulated water pump and a free surface tank. The pressure could be decreased in the system by means of a vacuum pump located in the tank. The operating point was characterized by the reference cavitation number σ_{ref} defined in the inlet reference section as:

$$\sigma_{\text{ref}} = \frac{P_2 - P_v}{0.5 \cdot \rho \cdot (U_1 - U_2)^2}, \tag{4}$$

where P_2 was the averaged pressure measured at the wall in the inlet section of the low speed flow and P_v was the vapor pressure which depends on the water temperature.

Downstream of the water pump, the flow was divided into two separated flows: in the following study, the high speed flow is referenced with the index 1 and the low speed flow with the index 2. Then, both flows crossed a settling chamber containing honeycomb frames and grids in order to homogenize the flow and to break large scale structures. Further on, the flows were accelerated in convergent pipes: boundary layers were then reduced to restrict the wake effect at the splitting plate tip. The convergent profiles have been optimized to avoid flow separation and cavitation at the wall.

The studied configuration was a traditional mixing layer. The inlet conditions were $U_1 = 15.8$ m/s for the high speed layer and $U_2 = 3.5$ m/s for the low speed layer (Fig. 1).

Five operating points with different cavitation levels were selected: one without cavitation (*no-cav*), one at inception (*cav*0) and three with developed cavitating structures (*cav*1–*cav*3). The corresponding cavitation numbers are presented in Table I. No σ_{ref} was defined for the case without cavitation, the cavitation number $\sigma_{\text{ref } no\text{-}cav}$ was set arbitrarily greater than $\sigma_{\text{ref } cav0}$ corresponding to the inception case.

The measurement of the water's temperature was required in order to calculate the vapor pressure and to set the selected cavitation number. The recorded water temperature varied within the range of 10–25°C depending on operating and atmospheric conditions.

The concentration of dissolved gas inside the water plays a major role in cavitation inception.[37] The experimental apparatus enabled us to measure but not to control the concentration of dissolved gas. The concentration of dissolved O_2 was acquired with an Orbisphere MOCA O_2 probe. A degasification protocol has been established in order to reach a minimum value of 3.5 ppm used for each operating point.

B. Dimensionless parameters

The aim was to analyze the self-similarity of the flow from velocity field measurements. Averaged velocity and fluctuations were considered. All parameters were dimensionless in order to be compared to values found in previous works on either compressible or incompressible fluids. The studied parameters are listed in the following nomenclature:

$$\Delta U = U_1 - U_2 \quad (\text{m/s}) \quad \text{Velocity shear}$$

$$U^* = \frac{U - U_2}{\Delta U} \quad (-) \text{ Dimensionless velocity}$$

$$U_i;\ V_i\,(m/s) \text{ Instantaneous velocity components}$$

$$u' = \sqrt{\frac{\sum_{i=1}^{n} (U_i - \bar{U})^2}{n}}\,(\text{m/s}),$$

$$u'^* = \frac{u'}{\Delta U} \quad (-) \quad \text{Longitudinal fluctuations}$$

$$n \text{ Sample size}$$

$$v' = \sqrt{\frac{\sum_{i=1}^{n} (V_i - \bar{V})^2}{n}}\,(\text{m/s}),$$

$$v'^* = \frac{v'}{\Delta U}(-) \quad \text{Transversal fluctuations}$$

$$u'v' = \frac{\sum_{i=1}^{n} (U_i - \bar{U})\,(V_i - \bar{V})}{n}\ (\text{m}^2/\text{s}^2)$$

$$u'v'^* = \frac{u'v'}{\Delta U^2}(-) \quad \text{Turbulent diffusion}$$

$$\begin{bmatrix} u'^2 & u'v' \\ u'v' & v'^2 \end{bmatrix} \quad (\text{m}^2/\text{s}^2) \quad \text{or } R_{ij} = 2k\left[b_{ij} + 1/3\ \delta_{ij}\right]$$

Cinematic Reynolds stress tensor (5)

$$k = \frac{u'^2 + v'^2 + w'^2}{2}\ (\text{m}^2/\text{s}^2) \text{ Turbulent kinetic energy}$$

$$b_{ij} = \frac{u'_i u'_j}{2k} - \frac{1}{3}\delta_{ij} \text{ where } u'_1 = u',\ u'_2 = v',\ u'_3 = w' \text{ Anisotropy tensor}$$

$$y* = \frac{y - y_{\text{ref}}}{\delta_\omega}(-)\ y\text{-coordinate where } y_{\text{ref}} \text{ is the center of the mixing area}$$

$$U(y_{\text{ref}}) = U_{\text{average}} = \frac{U_1 + U_2}{2}\ (\text{m/s}). \tag{6}$$

The splitting plate tip is located at $x = 0$ and $y = 0$. The location $y^* = \pm 1$ corresponds to the borders of the mixing area.

The separation wall between the two incoming flows was 6 mm thick and ended with a 5°symmetrical bevel. So, even with the 5:1 convergent pipes reducing the boundary layer thicknesses on the splitting plate sides, boundary layers remained 7 mm and 4 mm thick, respectively, on the high speed and low speed side at the tip of the splitting plate. A lack of momentum in the wake of the splitting plate remained. This momentum deficit was balanced by the momentum of the external layer, leading to a slight decrease of U_1 and U_2 in the wake of the splitting plate. The reference

TABLE I. Operating points.

	σ_{ref}
*cav*0	0.208 ± 0.007
*cav*1	0.167 ± 0.006
*cav*2	0.102 ± 0.004
*cav*3	0.012 ± 0.001

velocities remained $U_1 = 15.8$ m/s and $U_2 = 3.5$ m/s, but the local external velocities $U_1(x)$ and $U_2(x)$ were used to define the dimensionless parameters presented above.

C. Particle image velocimetry (PIV)

Velocity measurements have been performed using the 2D PIV–LIF technique in order to obtain the mean and fluctuating components of the velocity field of the liquid phase inside the two-phase part of the mixing layer. The PIV–LIF system was a LaVision DAVIS with a Twins Ultra Yag 2*30 mJ Laser with a light-sheet approximately 2 mm thick and wave length peak at 532 nm. An Imager ProX2 M camera with a minimum interframe time of 110 ns was used to record the PIV–LIF images.

The selected filter was a high-pass band at 570 nm and the corresponding particles were Rhodamine B type (20–50 μm diameter): it absorbs light at 532 nm and emits at 584 nm. A test pattern has been used to focus the devices on the middle vertical plan and to define the scale.

Five thousand pairs of pictures have been recorded by the acquisition system at each operating point. The delay between the two pictures was 120 μs ($\pm$ 0.05 μs accuracy). DAVIS 7.2 software was used to cross-correlate the pictures and give instantaneous velocity field for each pair of pictures. The resolution of the interpolation used for the determination of the correlation peak was sub-pixel ($\pm$ 0.05 pixel). The first pass interrogation area was 64×64 pixels followed by two passes with interrogation areas of 16×16 pixels. All passes had a 50% overlap. Velocity measurements were performed in the longitudinal section (x–y) in the middle plane of the mixing layer. The measurement area was 232 mm long and 71 mm high (Fig. 3).

A velocity vector was defined on each node of a 1.38 mm square mesh (160×52 vectors). None of the results were smoothed. The vectors rejected (without replacement) in the algorithm were those exceeding a difference to the average of twice the standard deviation of the nearest neighbors.

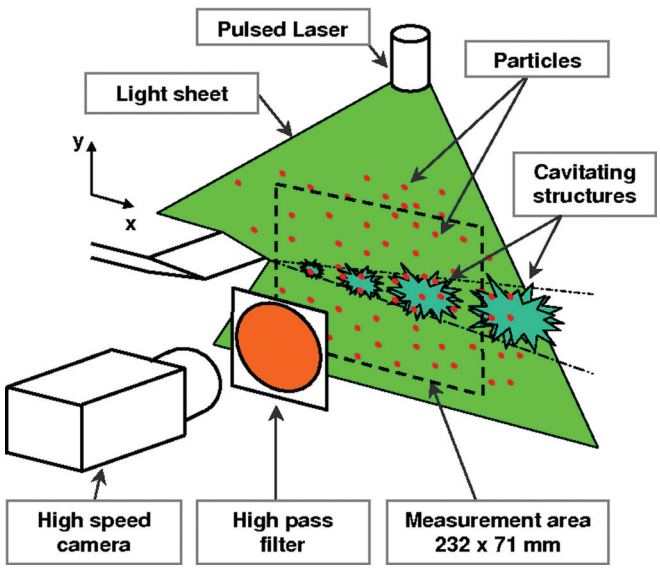

FIG. 3. (Color online) Location of the measurement area.

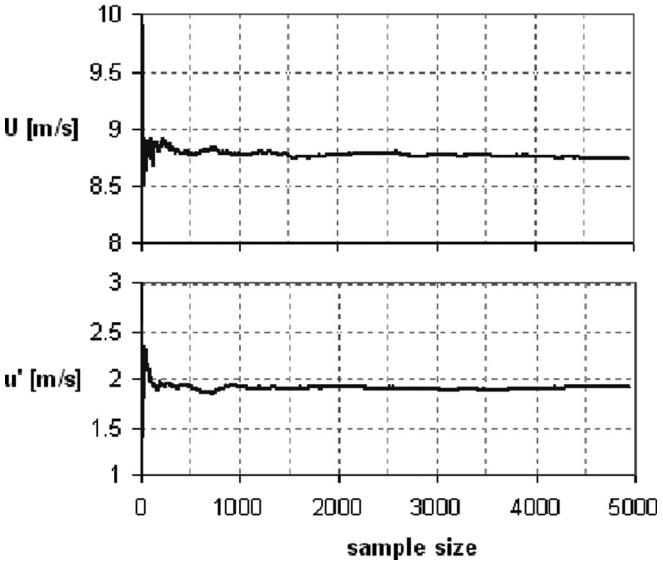

FIG. 4. Measurement convergence.

The statistical convergence of the velocity measurements has been studied over the whole measurement area: it showed that a minimum of 500 velocity vectors are needed to define the averaged velocity within a precision of $\pm$ 0.1 m/s and the standard deviation within $\pm$ 0.3 m/s. As an example, Fig. 4 presents the convergence curves obtained at the center of the mixing area ($y^* = 0$).

III. RESULTS AND DISCUSSION

A. Density and void ratio fields

X-ray absorption measurements have also been performed in this flow in order to obtain the mean and fluctuating density fields. Results are presented in great details in Aeschlimann *et al.*[30] X-Ray has been transformed to visible light by an x-ray image intensifier and the obtained visible light was captured by a high speed camera at a framing rate of 2 kHz with a shutter time of 20 μs in order to "freeze" the flow. The measurement area was 216×65 mm with a spatial resolution of 0.5 mm. For each operating point (*cav*1, *cav*2, and *cav*3) five image sequences of 8801 pictures were recorded, corresponding to a total observation time of 22 s. This data base lead us to obtain mean and fluctuating density (or volume fraction of vapor) fields.

Figures 5 and 6 show some examples of instantaneous images obtained during this experiment for the *cav*2 and *cav*3 cases, respectively. In these images the flow is from left to right, the horizontal axis is the longitudinal coordinate of the mixing layer (x) and the vertical one is the transversal coordinate with $x = 0$ mm and $y = 0$ mm corresponding to the splitting plate position. The grey scale value corresponds to the instantaneous local volume fraction value. For *cav*2 case, Kelvin-Helmholtz vortices clearly appear separated by pure liquid flow giving, even in the center of the mixing layer, an intermittent density field. At the opposite, for the *cav*3 case, vapor is always present in the mixing layer centerline.

It is possible to apply an averaging procedure to these data. Figure 7 shows an example of the mean volume fraction

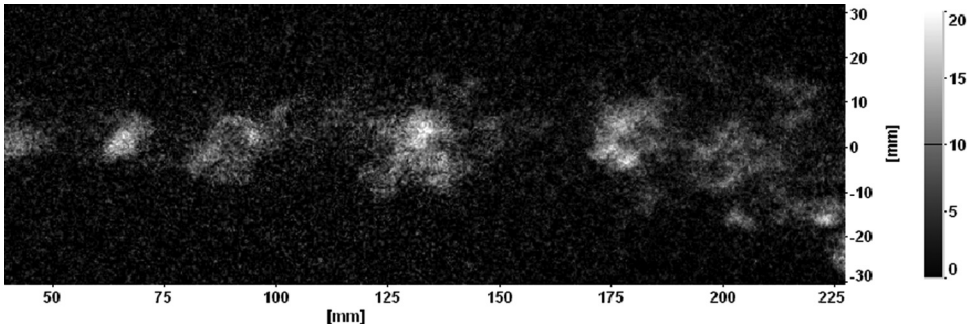

FIG. 5. Instantaneous volume fraction of vapor field (%)—*cav*2 (Ref. 30).

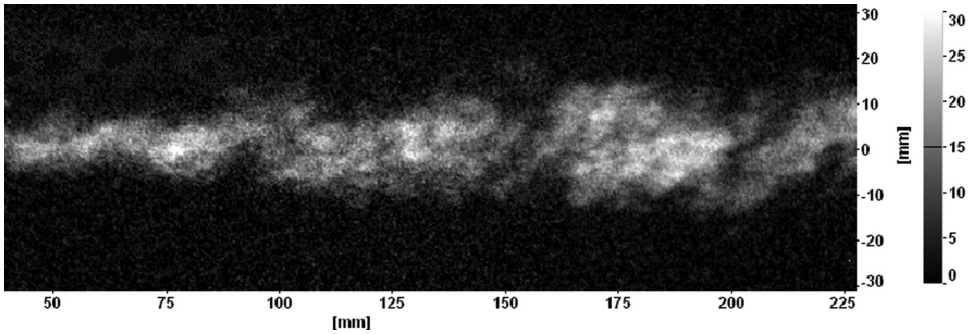

FIG. 6. Instantaneous volume fraction of vapor field (%)—*cav*3 (Ref. 30).

of vapor field for the *cav*3 case. An example of a typical mean profile is extracted for x close to 120 mm in the center of the self similarity zone. A bell type curve is then obtained. Both the mean and the fluctuating volume fraction of vapor fields exhibit a self similar behavior. To illustrate this fact, Fig. 8 shows the transversal evolution (in dimensionless transversal coordinate y^*) of the dimensionless mean values for a typical section in the self similar zone and for the three cavitating cases (*cav*1, *cav*2, and *cav*3). Similar plots concerning the relative standard deviation of the density fluctuations (σ_ρ/ρ, where $\rho = \alpha\rho_V + (1-\alpha)\rho_L$ is the density of the mixture) can be obtained as displayed on Fig. 9. Typical values for the maximum mean void ratio ranges from about 1% for *cav*1 to 3.5% for *cav*2 and finally 15% for *cav*3. Concerning the density fluctuations, typical maximum values range from 2% for *cav*1 to 4% for *cav*2 and finally 9% for *cav*3.

B. Averaged longitudinal velocity

From the averaged velocity fields, vertical velocity profiles, $U(y)$, were investigated. In order to qualify the mixing area and to analyze its self-similar behavior, 20 vertical profiles have been analyzed from x_2 to x_{21} locations, starting at $x_2 = 11.22$ mm with an 11.06 mm interval along x-axis.

Figure 10 shows some of these profiles for the *no-cav*, *cav*2, and *cav*3 cases. It is clear that the overall shape of all these profiles is qualitatively similar. No particular effect of the cavitating nature of the flow appears from a rough analysis of these profiles.

Dimensionless velocity profiles have also been plotted and superimposed separately for each operating point. For example, Fig. 11 presents $U^*(y^*)$ at the location $x = 121.8$ mm for each operating point (from *no-cav* to *cav*3). The self-preserving structure of the mean flow implies that $U^* = f(\eta)$, where η is the dimensionless coordinate; $\eta = y^*$ in the present study. The experimental results were compared to the analytic solution:[38]

$$f(\eta) = \frac{2}{\sqrt{\pi}} \int_{-\infty}^{\eta} e^{-(2x)^2} dx \tag{7}$$

$$\eta = \frac{y}{\delta_\omega} \tag{8}$$

A very good agreement was observed between each operating point and the analytic solution, confirming the self-preserving behavior of the mixing area development at this

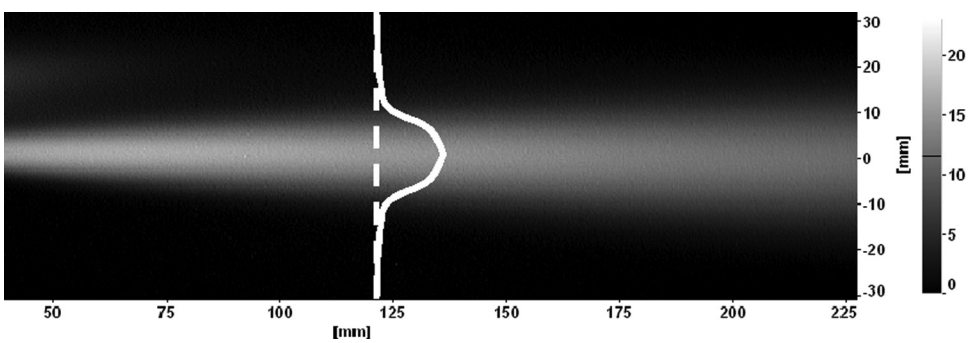

FIG. 7. Averaged void ratio (%)—*cav*3 (Ref. 30).

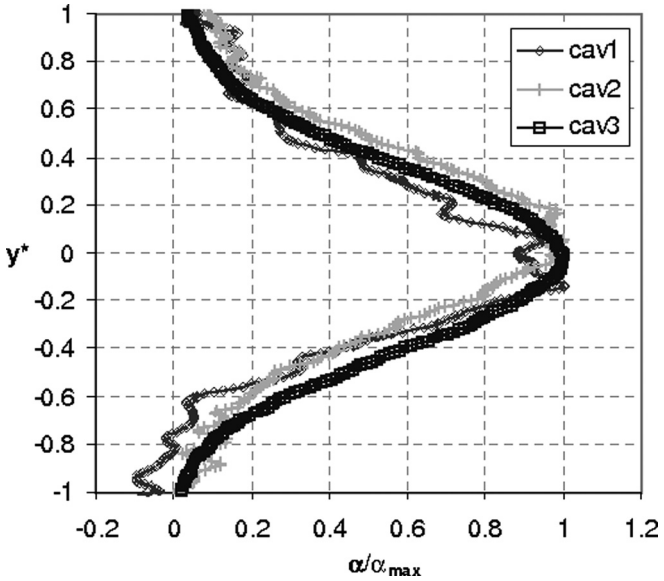

FIG. 8. Dimensionless mean void ratio profiles (Ref. 30).

longitudinal station. The main result is that the mean velocity profiles show that the self-similar behavior is also preserved despite the presence of the vapor phase. It should be noticed that in the wake of the splitting plate, the velocity profile did not match the analytic solution and this tendency is quite similar in cavitating cases. Therefore, a boundary between the self-similar area and a wake zone was defined at the location $x = 80$ mm and confirmed by the determination of the vorticity thickness.

In order to test the downstream limit of the self similar zone, a focus on velocity profiles in the downstream part of the flow was done. Figures 12(a) and 12(b) show a comparison between the dimensionless velocity profiles for the five studied cases and the self similar analytical solution for two positions in the downstream part of the flow ($x = 200$ and 221 mm).

If at $x = 200$ mm the overall tendency seems to confirm that the flow can still be considered as self similar, the results

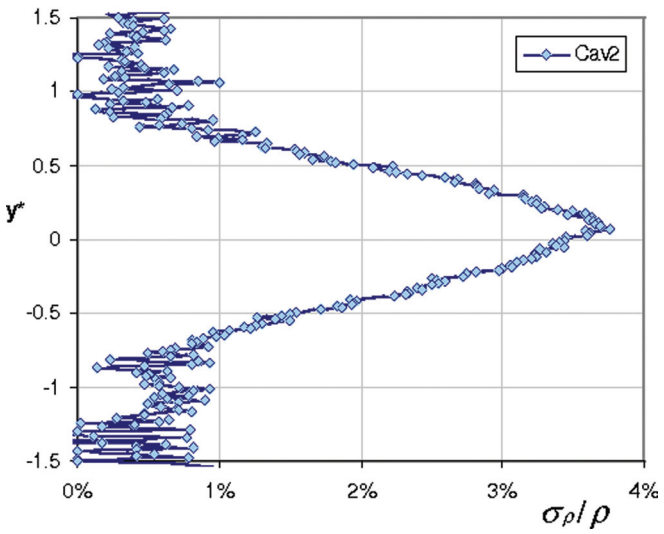

FIG. 9. (Color online) Transverse evolution of the relative standard deviation of the density fluctuations—*cav*2 (Ref. 30).

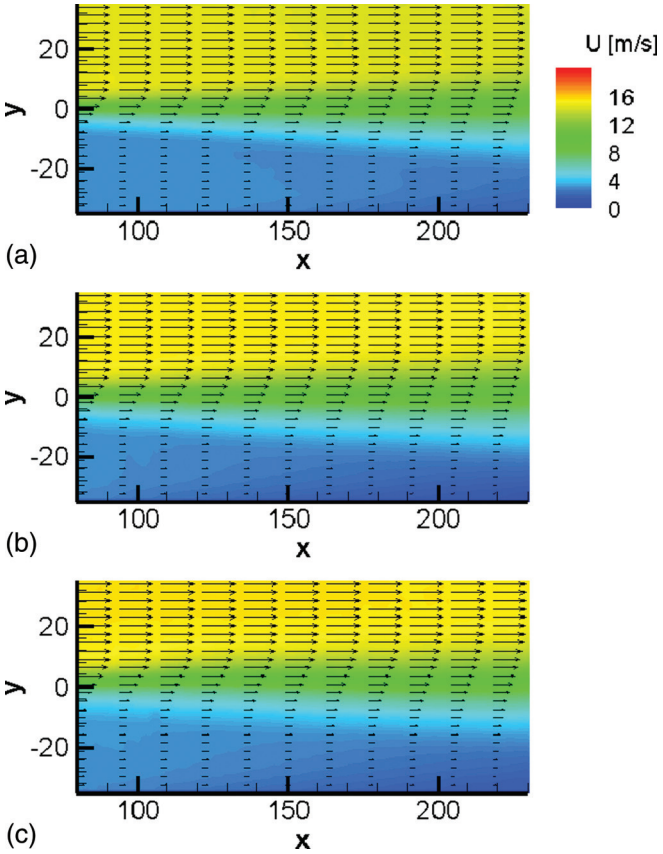

FIG. 10. (Color online) Mean averaged velocity profiles for (a) *no-cav*, (b) *cav*2, (c) *cav*3.

at $x = 221$ mm shows that the self similarity is not yet acceptable mainly on the low speed side of the flow. It has to be noted that at $x = 221$ mm (downstream side of the measurement area) the physical thickness of the mixing layer is about 64 mm ($\cong 2\delta_\omega$) for the most cavitating case (*cav*3). A crude estimation of the upper and lower wall boundary layer thicknesses[39] gave us values of 6.4 mm for the upper wall and 7.8 mm for the lower one. Then the total sheared zone at $x = 221$ mm is of the order of 78.2 mm for an outlet section height of 88.8 mm. The geometrical confinement appears

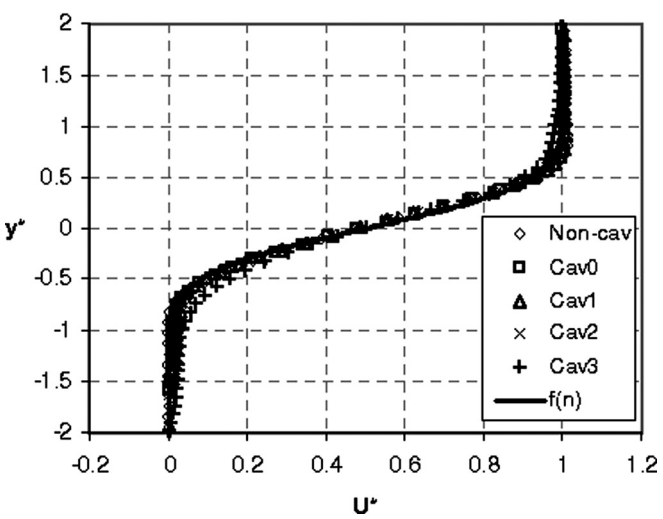

FIG. 11. Dimensionless velocity profiles: $x = 120$ mm.

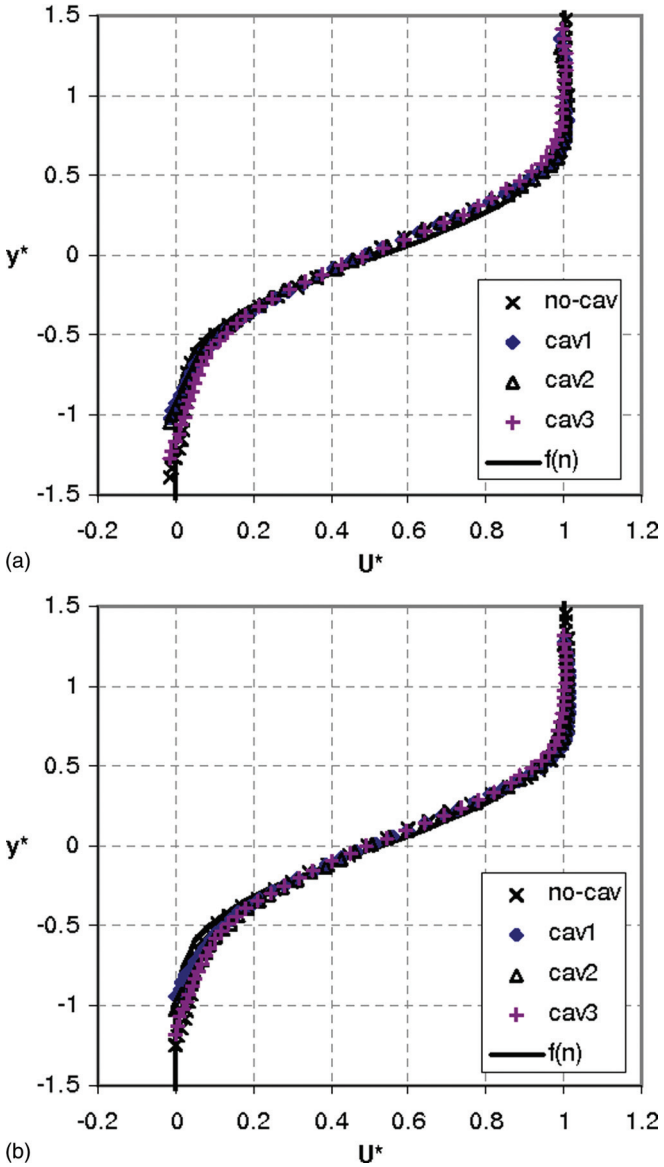

FIG. 12. (Color online) (a) Dimensionless velocity profiles: $x = 200$ mm. (b) Dimensionless velocity profiles: $x = 221$ mm.

rather large with a value close to 88%. However, as shown from dimensionless velocity profiles, the self similarity shape, if not exactly respected, is not entirely violated even with such huge confinement ratio of 88%. We can then conclude that the self similarity of the mixing layer velocity profiles is very robust with regard to the high confinement ratio it has to face. For the present study we can accept a rigorous self similar situation until $x = 200$ mm without any inconvenient. We then obtain a 120 mm range for the study of the self similar turbulent cavitating mixing layer.

C. Vorticity thickness and growth rate

The vorticity thickness characterizes the development of the Kelvin-Helmholtz instabilities at the interface of the layers. δ_ω grows linearly along the x-axis when the flow is self-similar.

From the mean velocity profiles, it was possible to define the longitudinal evolution of $\delta_\omega(x)$ which is plotted in Fig. 13 for each operating point. The dotted line marks the boundary of the self-similar area presented in the previous subsection. From $x_9 = 88.6$ mm, the linearity of the vorticity thickness along the x-axis is clearly visible for each operating point. It confirms that both the single phase flow and the cavitating flows were self-similar. The spatial development of the mixing area seems to be barely affected by cavitation.

Nevertheless, vorticity thickness seems greater, by about 30% in the cavitating cases than in the non-cavitating case. This behavior was due to the presence of vapor in the wake of the splitting plate leading to a wider vorticity thickness where the shear started to govern the flow. The main objective being to compare equivalent mixing layer developments, the wake effect of the splitting plate was corrected by an offset x_0 introduced in Eq. (9) in order to redefine an artificial origin of the mixing area:[24]

$$\delta_\omega = \delta'_\omega \times (x - x_0), \tag{9}$$

where the growth rate $\delta_\omega{}'$ is defined inside the self-similar area.

Values of $\delta_\omega{}'$ and x_0 are abstracted in Table II (the smallest coefficient of determination was obtained in the cav*3* case with $r^2 = 0.988$). The mixing layer autosimilar

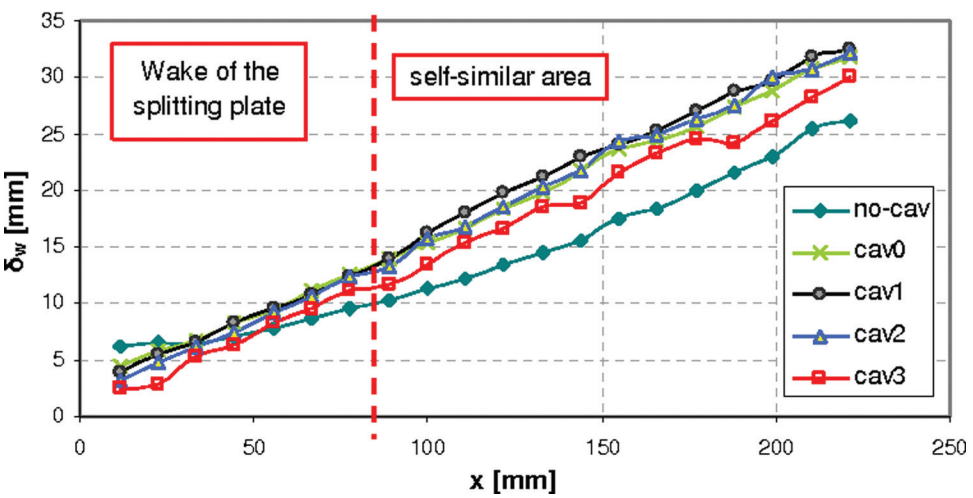

FIG. 13. (Color online) Vorticity thickness $\delta_\omega(x)$ evolution.

TABLE II. Mixing area development parameters.

	Case	δ_w'	X_0
1	*no-cav*	0.123	11.7
2	*cav*0	0.137	−12.7
3	*cav*1	0.137	−19.5
4	*cav*2	0.141	−9.9
5	*cav*3	0.133	−3.4

zone (which corresponds to the linear evolution of δ_ω versus x) is obtained more downstream in the non cavitating case than in cavitating ones. Figure 13 shows that a reminiscent wake evolution is clearly visible for the non cavitating case until $x \cong 80$ mm. Because of this situation the mixing layer is about 30% thicker in cavitating cases than in non cavitating ones. However this difference is not due to a 30% variation in mixing layer growth rate for the self similar zone but to a simple downstream translation of the self similar area in the non cavitating case.

In cavitating cases, the wake zone disappears very quickly (probably in less than 30 mm). It can be observed that, in these cases, a cavitating flow is already obtained on the upper part of the splitting plate. The main effect of this situation is an increase of the local turbulence levels, and consequently, the local mixing becomes stronger forcing the wake to collapse and creates the self-similar zone very rapidly with negative x_0 values. At the opposite, for non cavitating flows, the wake/mixing layer transition is harder to obtain. The shear layer thickness only evolves from $\delta_\omega \cong 6$ to 10 mm in the range between $x \cong 10$ and 80 mm. It is clear that the turbulence level is certainly lower in the upper part of the non cavitating flow making the wake/mixing layer transition more difficult than in cavitating situation. This effect is amplified by the relatively large thickness of the splitter plate (6 mm) compared to the initial one of the shear layer (less than 10 mm) making the initial wake more difficult to absorb. By combining these two effects we obtain a positive value for x_0.

With these results we compared cavitating and non-cavitating cases at a constant x–x_0 in order to compare dimensionless parameters. The growth rate is not clearly modified by the presence of the vapor phase and the cavitating mixing area development is similar to that obtained in a single phase flow.

The non-exhaustive overview of the studies of turbulent incompressible and compressible mixing layers highlighted that δ_ω' is a function of the fluid properties and the inlet conditions[24] and many authors introduced a function defined as follows:

$$\delta_\omega' = \delta_\omega'(r,s), \tag{10}$$

where $r = U_2/U_1$ and $s = \rho_2/\rho_1$.

In the present study, both layers were liquid water and therefore $\rho_2/\rho_1 = 1$, so $s = 1$. Thus $\delta_\omega'(r,s)$ was reduced to

$$\delta_\omega' = C\frac{1-r}{1+r}, \tag{11}$$

where C is a constant defined experimentally with a downward facing step flow where $r = 0$ and therefore $\delta_\omega' = C$.

Dimotakis[40] defined C in the range of 0.16–0.18. Brown *et al.*[24] recommended $C = 0.181$. According to the bibliography, experimental values vary within a range of ± 20% of this last value for all the tested incompressible flows. Referring to compressible flows, with equivalent s and r, vorticity thickness would be about five times less.[24,25]

We noticed that the operating point without cavitation followed Brown *et al.*[24] results within less than 10%. Regarding the cavitating cases, results were also included in the ± 20% range of values concerning incompressible mixing layers.

Considering those first results, we concluded that the self-similarity of the mean flow was preserved, inducing a similar development of Kelvin-Helmholtz instabilities in the cavitating cases. Even if x_0 differed from one case to the other, the main parameter remained the growth rate δ_ω' which was steady despite the development of cavitation. No major changes to the mean flow were observed when cavitation developed, and no compressibility effects, such as an attenuation of the development of Kelvin-Helmholtz instabilities were observed.

The following part will now focus on the analysis of the velocity fluctuations.

D. Turbulent shear flow

1. Velocity fluctuations

Fluctuations of the velocity field have been analyzed. Figure 14 presents an example of the longitudinal fluctuations u'^* at a location inside the self-similar area for different operating points. Transversal fluctuations (u' and v') and turbulent diffusion ($|u'v'|$) profiles had similar shapes: outside the mixing area ($y^* > 1$ and $y^* < -1$), low and constant values of u', v' and $u'v'$ were measured and maximum values were reached at the center line of the mixing area ($y^* = 0$).

Concerning the non-cavitating case and regarding the previous results, turbulent fluctuations are in a good

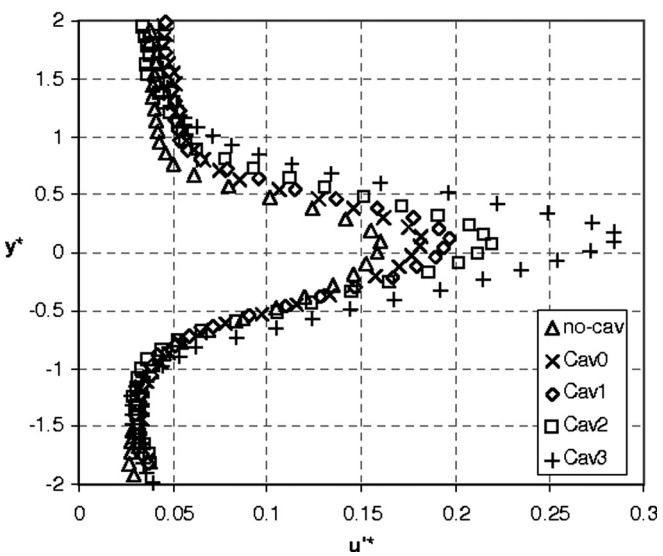

FIG. 14. Longitudinal velocity fluctuations: u'^*, $x - x_0 = 120$ mm.

agreement with the results of Liepmann *et al.*,[41] Wygnansky *et al.*,[42] Patel,[43] and Browand *et al.*[44] concerning incompressible flows. Regarding the compressible flows, the review presented in Barre *et al.*[45] highlighted a tendency of a 50% decrease of both the longitudinal fluctuations u'^* and the turbulent diffusion $u'v'^*$.

In the cavitating regime, the development of the vapor phase led to an increase of u′* which differs from both the compressible and incompressible tendencies of one-phase flows. This trend was more pronounced when the cavitation index was decreased particularly, for the *cav*3 case where u'^* increased by about 80% at $x–x_0 = 120$ (Fig. 14).

In order to analyze the fluctuation evolutions, longitudinal profiles were studied for each operating point. The longitudinal and transversal fluctuations (u'^* and v'^*) and the maximum turbulent diffusion ($u'v'^*$) are presented in Figs. 15–17; the dots are linked where the mean velocity profiles were self-preserved: $x > 80$ mm.

In Fig. 15, concerning the non-cavitating case, we observed that u'^* strongly decreased in the wake of the splitting plate before stabilizing at $x = 80$ mm. The longitudinal fluctuations u'^* were steady inside the mixing area where the mean flow was self-preserved, agreeing with the standard mixing layer analysis. However, regarding the cavitating cases, due to vapor production and bubble collapse, u'^* and v'^* increased when cavitation developed. Longitudinal fluctuations were particularly affected. For example, at $x - x_0 = 145$ mm, comparing *no-cav* and *cav*3 cases, u'^* increased by 63% whereas v'^* increased only by 36%. Moreover, v'^* values seemed steady for each operating point, while u'^* decreased continuously along the x-axis.

The turbulent diffusion $u'v'^*$ was null outside the mixing area ($y^* > 1$ or $y^* < -1$), this was typical of isotropic and homogeneous turbulence. However, inside the mixing area, U and V were correlated due to the vortex dynamic. $u'v'$ values were negative, the maximum of its absolute value was

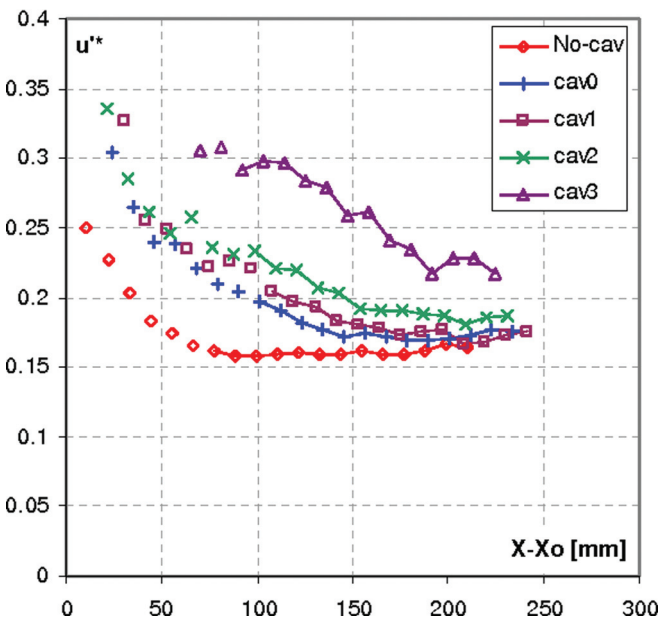

FIG. 15. (Color online) Maximum longitudinal velocity fluctuations: u'^*, $y^* = 0$.

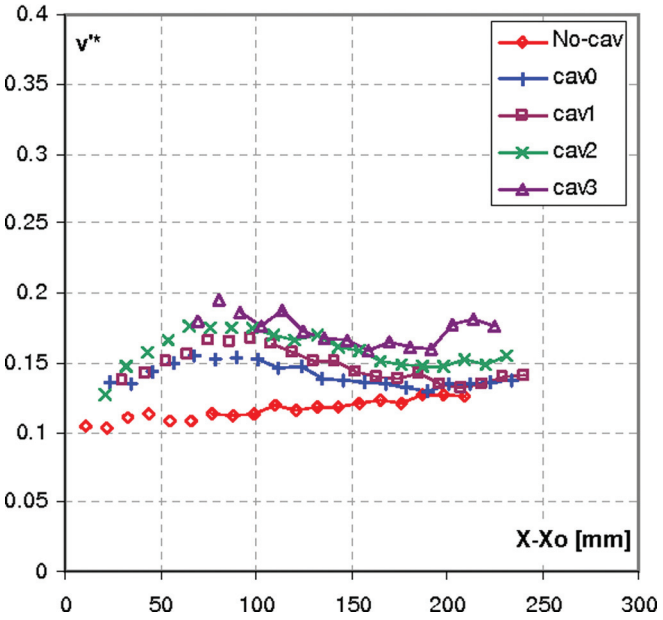

FIG. 16. (Color online) Maximum transverse velocity fluctuations: v'^*, $y^* = 0$.

reached at the center of the mixing area ($y^* = 0$). No noticeable evolution was observed when the cavitation number was decreased and $u'v'^*$ stayed almost constant along the x-axis.

Longitudinal fluctuations had greater amplitude than transversal ones, a tendency that was also observed in every typical sheared flow, such as boundary layers or wake flows. Gopalan *et al.*[33] noticed that longitudinal fluctuations increased in the reattachment area of a flow separation where cavitation collapsed, compared to the non-cavitating flow. Iyer *et al.*[28] also noticed a 15% increase of u'^* in the downstream part of a cavitating mixing layer where two-phase structures collapsed. Those two examples highlighted the influence of cavitation on velocity fluctuations where the complete implosion of the two-phase structures occurred. This was not representative of the mixing layer development but it suggested that vapor destruction leads to an increase of

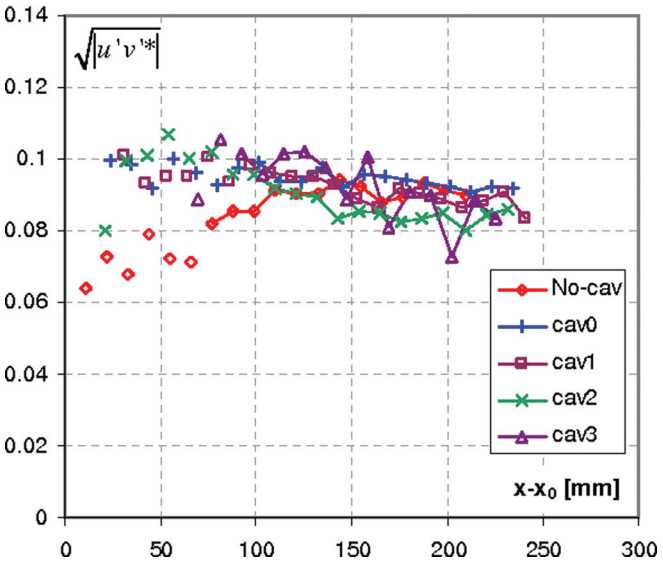

FIG. 17. (Color online) Maximum turbulent diffusion : $y^* = 0$.

the longitudinal fluctuations. As seen in Aeschlimann *et al.*,[30] vapor structure evolution along the x-axis in the mixing area was not simply vapor production. It was a complex combination of the creation of vapor bubbles coupled with their collapse. Thus vaporization and condensation of the fluid particles led to additional fluctuations. Since turbulent diffusion was not affected by cavitation, it seemed that the cavitation was carried along within the vortices without changing their global dynamic.

From the velocity fluctuation analysis, we concluded that there was no evolution of the turbulent diffusion $u'v'^*$ when cavitation was increased. The averaged u'^* and v'^* increased significantly between the non-cavitating (*no-cav*) and highly cavitating (*cav*3) working points. The net effect of compressibility, as it is known in compressible gas flow, was not observed when cavitation developed inside the mixing area. Furthermore, the fluctuations u'^* and v'^* differed also from incompressible references.

From these results, Reynolds tensor components were characterized over the range of σ_{ref} studied. It will be used as a reference to validate turbulence models with numerical simulations.

2. Turbulent kinetic energy

In order to better understand this induced production of turbulence in the privileged direction while the mean motion is not affected, let us consider the anisotropy tensor evolution, characteristic length scales, and the turbulent diffusivity. These parameters allowed additional information concerning the eddy shape evolution in the two-phase mixing layer.

The kinetic energy is the sum of the three components u'^2, v'^2 and w'^2. The third one is the fluctuations of the third component of the velocity, W, which was not measured during this PIV–LIF campaign. Wygnanski *et al.*[42] measured w' in a downward facing step (flow without cavitation). w' has been compared to u': $w'/u' = 0.85$. This was the ratio used to estimate the missing component of the kinetic energy k presented as an example in Fig. 18 at the location $y'^* = 0$ and $x - x_0 = 145$ mm.

The kinetic energy was maximal at the center of the mixing area as it was expected through the previous turbulent intensity evolutions. Evolution of kinetic energy with cavitation index is plotted and compared to the value in the *no-cav* case. The kinetic energy had doubled at $y^* = 0$ and $x - x_0 = 145$ mm between the flow without cavitation and the most cavitating one. This global result was instructive but not representative of the anisotropy effects due to the vapor phase previously observed on the turbulent intensity distributions. In order to take into account inter-component energy transfer and spatial redistribution of the energy, it is necessary to consider the Reynolds stress tensor which depends on the dynamics of the turbulent flow. The simplest model is the isotropic one but the most realistic one is the one obtained using the decomposition into two parts (5) given by Lumley *et al.*[46] This decomposition introduces a symmetric term and a deviatoric term and has been investigated in the present paper in order to highlight the cavitation effects on the spatial redistribution of turbulent energy.

3. Anisotropy tensor

The evolution of the four main terms of the anisotropy tensor for each working point was analyzed at the location $y^* = 0$ and $x - x_0 = 145$ mm (Fig. 19). b_{11} and b_{33} were linked because w' fluctuations were deduced from u' using a constant factor ($w'/u' = 0.85$).

When σ_{ref} decreased, the longitudinal part of the fluctuations contained in the global turbulent kinetic energy k increased significantly from $\sigma_{ref} = 0.102$ (*cav*2). The growth from u' (b_{11}) was followed by the decrease of v' (b_{22}).

We observed therefore a major change in the evolution of anisotropy between *cav*2 and *cav*3 cases (Fig. 19). However, the ratio between the turbulent shearing rate and the turbulent kinetic energy (b_{12}) grew continuously, mainly due to the constant increase of k because, as we have seen, the turbulent shearing ($u'v'$) was quasi-constant over the range of σ_{ref} studied. As a result, the Reynolds tensor was modified as cavitation developed and especially from *cav*2. The cavitation effect increased the turbulent fluctuation rate without changing the turbulent shearing rate.

In turbulence modeling, the parameter $\frac{|u'v'|}{k}$ is classically used as a reducer factor. The well-known Bradshaw hypothesis, applied to one-phase two-dimensional experimental

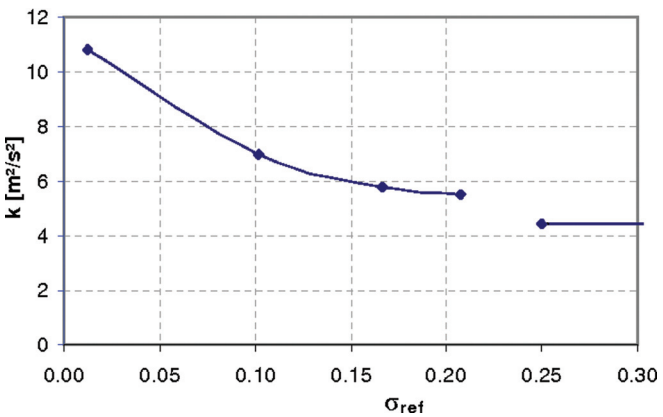

FIG. 18. (Color online) Kinetic energy in the self-similar area ($y^* = 0$, $x - x_0 = 145$ mm).

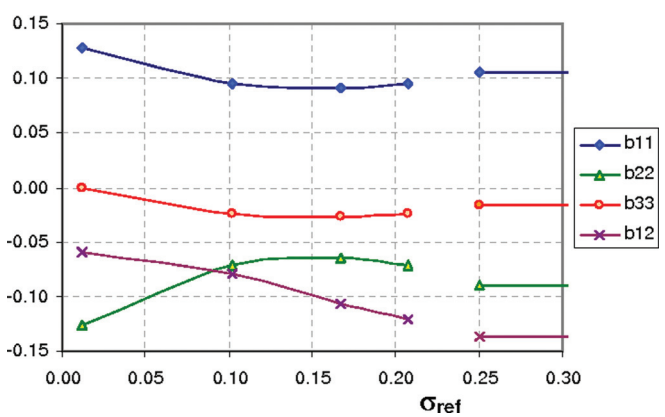

FIG. 19. (Color online) Anisotropy tensor components ($y^* = 0$, $x - x_0 = 145$ mm).

flows, suggests an equilibrium area between production and dissipation and gives,

$$2b_{12} = \frac{|u'v'|}{k} \leq 0.3. \quad (12)$$

We noticed that Bradshaw's hypothesis is verified in the present experiment for all operating points, whether cavitating or not. $\frac{|u'v'|}{k}$ decreased significantly and continuously when cavitation developed (we observed a coefficient of 2 between *no-cav* and *cav*3*)*. Thus the turbulence production level represented by $u'v'$ was more efficiently converted to turbulent kinetic energy when cavitation was strongly developed.

4. Discussion

This experimental study has been conducted in order to define a test case where the influence of cavitation on turbulence could be analyzed in detail. Another interest of the data obtained was for it to be used to validate numerical simulations. Refined measurements of Reynolds stresses and velocity gradients made it possible for us to determine the eddy viscosity coefficient, mainly used to close cavitating flow models. The standard Boussinesq viscosity hypothesis is defined as the ratio of the Reynolds stress by the mean strain rate in the same plane:

$$\mu_t = -\rho \frac{u'v'}{\frac{\partial U}{\partial y}}. \quad (13)$$

This hypothesis expressed by Eq. (13) assumes that the turbulent diffusion is isotropic and may not be suitable for many complex flows involving strong three-dimensional effects and it is delicate to properly describe all turbulent flows where large scale structures are predominant. This is the reason why the present discussion attempts to validate the Boussinesq hypothesis in the case of the cavitating shear layer.

As seen in the mixing layer flow presented here, even without cavitation, the turbulent fluctuations were anisotropic:

$$u' > v'. \quad (14)$$

This tendency was amplified with the development of two-phase structures where the longitudinal fluctuation and diffusivity were favored. Few studies performed corrections, see for example Bourguet *et al.*[47] where an eddy viscosity tensor was implemented in the model.

The second problem came from the compressible effect of the two-phase structures on the flow. As shown in this study, the compressibility effect on the mean velocity field and fluctuation behaved differently from the net effect of compressibility observed in one-phase supersonic flows.[25,26] The compressibility of the mixture had to be taken into account. This was achieved by using a correction or by adding parameters leading to a noticeable decrease of the eddy viscosity. For example, an empirical formulation was established by Coutier *et al.*[16] in a k-ε RNG model:

$$\mu_t = f(\rho) C_\mu k^2/\varepsilon \quad (15)$$

with

$$f(\rho) = \rho_v + (1-\alpha)^n(\rho_l - \rho_l);\ n = 10;\ C_\mu = 0.085 \quad (16)$$

where

- α is the void ratio;
- ε is the turbulent dissipation;
- k is the turbulent energy;
- ρ_v and ρ_l are the vapor and liquid densities.

This correction was based on the void ratio and has been used for example by Dular *et al.*,[31,32] or Coutier *et* al.[16] in attached cavitation sheet around a hydrofoil.

Using Eq. (13), it was possible to estimate experimentally the eddy viscosity μ_t. In fact, the present experimental eddy viscosity is comparable to the one which will be obtained at the end of a temporally converged simulation result. The density ρ of the two-phase structure was estimated in a previous work conducted by Aeschlimann *et al.*[30] As an example, the Fig. 20 presents the eddy viscosity for the studied operating points (the averaged void ratio is tagged). In order to obtain the experimental turbulent viscosity the lateral Reynolds stress $\overline{u'v'}$ was averaged using the entire PIV–LIF data set and then multiplied by the average density. To illustrate the effect of the correction (15), the limiter function $f(\rho)$ (16) was used instead of ρ in Eq. (13) to estimate the value of the eddy viscosity which will be used with the Reboud model to correct the present experimental values in the case of a numerical simulation. This is done in two ways. The first one by performing the correction using Eq. (16) and then computing $f(\rho)$ for each temporal data available and then averaging at the end (model 1). This procedure is the rigorous one because it corresponds to the average of $f(\rho)$. The second way of computing the correction function was by simply applying Eq. (16) using the mean value of the void ratio (model 2). This procedure is non rigorous but has been applied to test the effect of the non linearity of the corrective function on the value of the obtained correction. Figure 20 shows the evolution of both the experimental values and the corrected values with models 1 and 2 averaging techniques. The measured μ_t decreased slightly with cavitation development. However, the effect of the

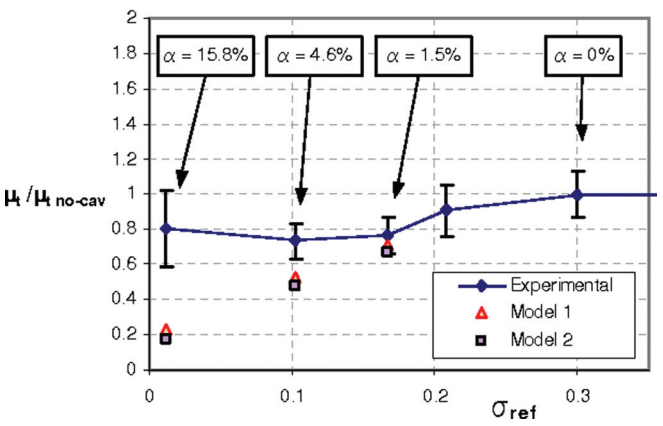

FIG. 20. (Color online) Turbulent viscosity versus cavitation number (x = 120 mm, $y^* = 0$)

cavitation on the turbulent viscosity was voluntarily overestimated by the corrected model used in numerical simulation. The limiter (16) led to a fast artificial decrease of μ_t as soon as the vapor started to appear. Furthermore, this correction seems to be poorly affected by the averaging technique used to compute the function $f(\rho)$.

It is commonly observed in numerical analysis that unsteadiness hardly occurs without such modifications.[16,36] Numerical simulations were validated with experimental measurements, mainly comparing apparent two-phase structure sizes and shedding frequencies. The Reboud correction lead the simulation to obtain a good frequency shedding for the cavitating structures which are ejected at the rear part of the cavitating sheet. This is especially the case for venturi flows. It seems that this correction mainly manages the turbulent boundary layer detachment dynamics at the rear part of the venturi cavitation sheets. In the present case (2D mixing layer), taking into account the absence of wall and detachment, it is not so surprising that this correction did not work as well.

5. Integral scale

Spatial correlation of the longitudinal velocity was analyzed in order to define a coherent size of the vortices and the spatial diffusivity with the cavitation process. Longitudinal and transversal correlations were estimated from $y=0$ mm and $x=120$ mm:

$$R_{U,x}=\frac{\overline{(U(x,y)-\overline{U(x,y)})\times(U(x+dx,y)-\overline{U(x+dx,y)})}}{u'(x,y)\times u'(x+dx,y)}, \tag{17}$$

$$R_{U,y}=\frac{\overline{(U(x,y)-\overline{U(x,y)})\times(U(x,y+dy)-\overline{U(x,y+dy)})}}{u'(x,y)\times u'(x,y+dy)}. \tag{18}$$

Figure 21 displays the transversal correlation $R_{U,y}$. Longitudinal correlation had a similar shape: starting at 1 where the signal was compared to itself ($dx=0$ mm or $dy=0$ mm) and rapidly decreasing, tending to 0, where the shift (dx or dy) increased.

From the spatial correlations, characteristic vortex length scales were defined by integrating the profiles. The dimensionless form of the integral scale was adapted for comparison with the vorticity thickness,

$$L_x^*=\int_0^{2\delta_\omega} R_{U,x}d\left(\frac{dx}{\delta_\omega}\right), \tag{19}$$

$$L_y^*=\int_0^{2\delta_\omega} R_{U,y}d\left(\frac{dy}{\delta_\omega}\right). \tag{20}$$

Longitudinal and transversal integral scales are presented in Fig. 22 for the studied cavitation levels. Both scales decreased with the cavitation development. The longitudinal scale seemed to stop decreasing from $\sigma_{\mathrm{ref}}=0.167$ ($cav1$) at

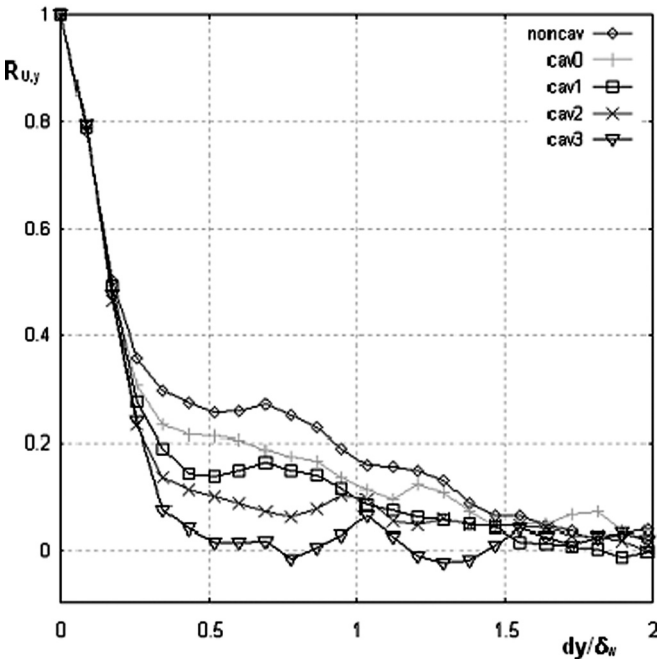

FIG. 21. Spatial correlation of the longitudinal velocity.

about $L_x=0.35$ δ_ω while L_y kept decreasing, reaching $L_y=0.21$ δ_ω for the most cavitating case ($cav3$).

When no vapor was present, L_x* and L_y* had the same magnitude, $L_x=L_y=0.45$ δ_ω, meaning the vortex structures had a cylindrical shape. However, when cavitation develops, the structures change shape. The shape factor ratio L_x/L_y gives an overview of the vortex shape evolution. From $\sigma_{\mathrm{ref}}=0.167$ ($cav1$) up to $\sigma_{\mathrm{ref}}=0.012$ ($cav3$), the shape factor grows, respectively, from 1.03 to 1.56: the vortices appear to be flattened, privileging the longitudinal direction; but due caution has to be taken here, no inclination of the ellipsoidal

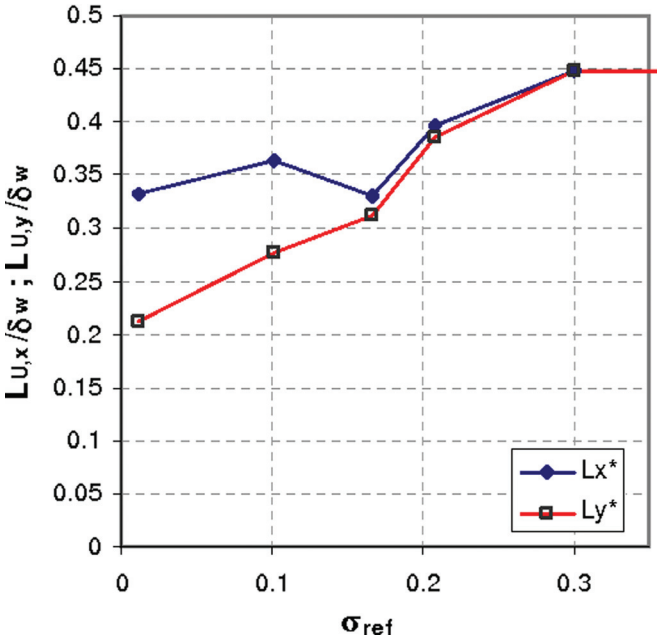

FIG. 22. (Color online) Dimensionless integral scales based on the longitudinal velocity.

vortices were estimated in the present study. Sridhar *et al.*[48] studied convected bubbles in vortex rings. They also observed an initial circular vortex when no vapor was injected in the flow; then, when bubbles appeared inside the vortices, these were distorted from their initial circular shape to an ellipsoidal shape. Marginal or major distortions were differentiated depending on the void ratio. Wygnanski *et al.*[42] also measured integral scales in a mixing layer, results showed self-preserved values of L_x and L_y along $y^*=0$ and besides, the vortex shapes were not cylindrical. Wygnanski *et al.*[42] estimated $L_x=0.57\ \delta_\omega$, and $L_y=0.31\ \delta_\omega$ in a one-phase gas flow. This distortion could result from the curvature of the mixing area due to the absence of the secondary flow ($U_2=0$ m/s).

The growth of velocity fluctuations due to cavitation development did not lead the coherent structures to grow. It seems that the extra-fluctuations present in the vortex cores were random and uncorrelated to the main dynamic of the Kelvin-Helmholtz instability.

From characteristic lengths of the structure, such as the integral scales L_x and L_y and the turbulent fluctuations u' and v', we can define a turbulent diffusivity,

$$D_T = L \times u'(\mathrm{m}^2/\mathrm{s}). \tag{21}$$

The turbulent diffusivity could be interpreted and compared to the molecular diffusivity mechanism, but unlike the molecular diffusivity, D_T is not a fluid property, but depends on the flow characteristics. Figure 23 presents the D_T based on the cross-stream and streamwise measures for different cavitation levels (location $y^*=0$ and $x=120$ mm). An anisotropic tendency of the turbulent diffusivity is observed for the range of σ_{ref} studied. The longitudinal turbulent diffusivity was 40% greater than the transversal turbulent diffusivity in the non-cavitating case ($\sigma_{\mathrm{ref}}>0.3$), and about 150% greater in the most cavitating case. We observed that cross-stream D_T was steady with a slight decrease with the cavitation development while the streamwise D_T increased by 65%. So, the two-phase structures led to a reduction of the coherent size of the vortices and, in the meantime, vapor bubbles increased the turbulence rate and the diffusivity, adding random fluctuations.

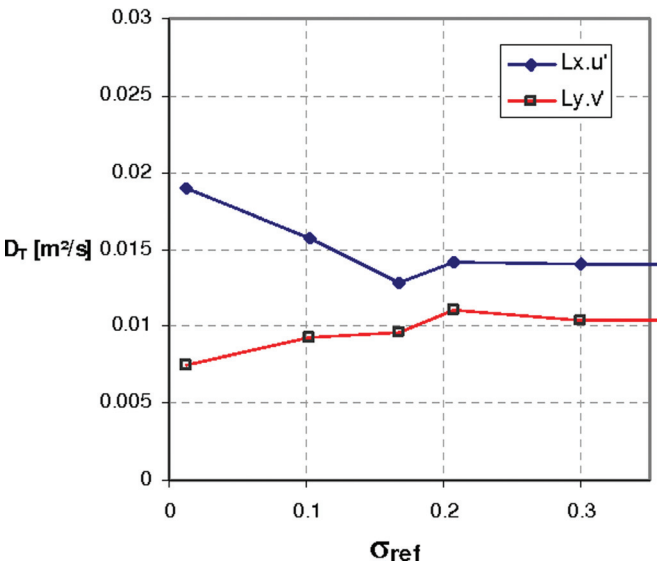

FIG. 23. (Color online) Turbulent diffusivity ($x=120$ mm, $y^*=0$).

IV. CONCLUSION

Velocity measurements were performed with a PIV–LIF system in a 2D cavitating shear layer flow. Acquisition of instantaneous velocity fields allowed us to analyze the dynamic of a mixing layer flow.

Convergence analysis of the measurements has validated the statistical results up to the second order moment. The average velocity fields and its fluctuations were acquired and analyzed.

The dimensionless analysis of mean velocity profiles enabled us to identify the self-preserved flow zone. Parameters that characterized the flow dynamic were studied and quantified: vorticity thickness, growth rate, Reynolds tensor components, and integral scales. Turbulent kinetic energy and the anisotropy tensor components were also estimated and analyzed. Once coupled with the void ratio measurements, the turbulent diffusion led to the turbulent viscosity inside the mixing area. These parameters will be used as references for validation of turbulence models with numerical simulations.

General behaviors have been observed: a turbulent shear area along the x-axis developed, growing linearly, showing a constant growth rate over the studied cavitation levels. The main results of this study showed clearly that the turbulence-cavitation relationship inside a mixing layer is not simply a change of compressibility properties of the fluid in the turbulent field due to the presence of a two-phase flow. We observed phenomena different to those observed in one-phase compressible flows, so physical properties of one-phase supersonic flows could not be used for cavitation effect analysis.

The mean velocity field was not affected by cavitation, however, the successive vaporization and collapsing of bubbles added additional fluctuations, mostly longitudinal, while the turbulent diffusion remained constant. As the cavitation developed, the coherent sizes of the vortices decreased without reducing the mixing area thickness.

ACKNOWLEDGMENTS

The authors wish to express their gratitude to the French Space Agency (CNES) and the rocket engine division of Snecma for its continuous support. Technical support by L. Vignal (LEGI, Grenoble, France).

[1]S. Barre, J. Rolland, G. Boitel, E. Goncalves, and R. Fortes-Patella, "Experiments and modeling of cavitating flows in Venturi: Attached sheet cavitation," Eur. J. Mech. B/Fluids **28**, 444 (2009).
[2]R. T. Knapp, J. W. Daily, and F. G. Hammitt, *Cavitation* (McGraw-Hill, New York, 1970).
[3]J. Katz, "Cavitation phenomena within regions of flow separation," J. Fluid Mech. **140**, 397 (1984).
[4]G. Wang, M. Shintani, S. J. Liu, B. R. Shin, and T. Ikohagi, "Cavitation characteristics around a hollow-jet valve (Observation by high-speed photographs and monitoring by vibration)," Trans. Jpn. Turbomach. Soc. **26**, 361 (1998).
[5]J. Katz and T. O'Hern, "Cavitation in large scale shear flows," J. Fluids Eng. **108**(3), 373 (1986).

[6]G. Wang, S. Liu, M. Shintani, and T. Ikohagi, "Study on cavitation damage characteristics around a hollow-jet valve," JSME Int. J., Ser B **42**(4), 649 (1999).
[7]R. W. Kermeen and B. R. Parkin, "Incipient cavitation and wake flow behind sharp-edged disks," California Institute of Technology Hydrodynamics Laboratory Report No. 85-4, 1957.
[8]J. O. Young and J. W. Holl, "Effects of cavitation on periodic wakes behind symmetric wedges," J. Basic Eng. **88**(1), 163 (1966).
[9]B. Belahadji, J. P. Franc, and J. M. Michel, "Cavitation in the rotational structures of a turbulent wake," J. Fluid Mech. **287**, 383 (1995).
[10]B. Stutz and J.-L. Reboud, "Two-phase flow structure of sheet cavitation," Phys. Fluids **9**, 3678 (1997).
[11]B. Stutz and J.-L. Reboud, "Measurements within unsteady cavitation," Exp. Fluids **29**, 545 (2000).
[12]T. M. Pham, F. Larrarte, and D. H. Fruman, "Investigation of unsteady sheet cavitation and cloud cavitation mechanisms," J. Fluids Eng. **121**(2), 289 (1999).
[13]A. Kubota, H. Kato, H. Yamauchi, and M. Maeda, "Unsteady structure measurement of cloud cavitation on a foil section using conditional sampling techniques," J. Fluids Eng. **111**, 204 (1989).
[14]Q. Le, J. P. Franc, and J. M. Michel, "Partial cavities: Global behavior and mean pressure distribution," J. Fluids Eng. **115**(2), 243 (1993).
[15]Y. Kawanami, H. Kato, H. Yamaguchi, M. Tanimura, and Y. Tagaya, "Mechanism and control of cloud cavitation," J. Fluids Eng. **119**, 788 (1997).
[16]O. Coutier, B. Stutz, A. Vabre, and S. Legoupil, "Analysis of cavitating flow structure by experimental and numerical investigations," J. Fluid Mech. **578**, 171 (2007).
[17]W. Hassan, S. Legoupil, D. Chambellan, and S. Barre, "Dynamic localization of vapor fraction in turbopump inducers by x-ray tomography," IEEE Trans. Nucl. Sci. **55**(1) Pt. 3, 656, 2008.
[18]K. Yokota, K. Kurahara, D. Kataoka, Y. Tsujimoto, and A. J. Acosta, "A study of swirling backflow and vortex structure at the inlet of an inducer," JSME Int. J. Ser. B **42**(3), 451 (1999).
[19]X. Qiao, H. Horiguchi, and Y. Tsujimoto, "Response of backflow to flow rate fluctuations," J. Fluids Eng. **129**, 350 (2007).
[20]N. Yamanishi, S. Fukao, X. Qiao, C. Kato, and Y. Tsujimoto, "LES simulation of backflow vortex structure at the inlet of an inducer," J. Fluids Eng. **129**, 587 (2007).
[21]T. Hashimoto, T. Komatsu, K. Kamijo, S. Hasegawa, M. Watanabe, and H. Yamada, "Observation of backflow and prewhirl at rocket propellant pump inducer," AIAA Paper No. 2000 (2000).
[22]K. Okita, H. Ugajin, and Y. Matsumoto, "Numerical analysis of the influence of the tip clearance flows on the unsteady cavitating flows in a three-dimensional inducer," J. Hydrodynam. **21**(1), 34 (2009).
[23]K. Yokota, K. Mitsuda, Y. Tsujimoto, and C. Kato, "A study of vortex structure in the shear layer between main flow and swirling backflow," JSME Int. J., B **47**(3), 541 (2004).
[24]G. Brown and A. Roshko, "On density effects and large structure in turbulent mixing layers," J. Fluid Mech. **64**, 775 (1974).
[25]D. Papamoschou and A. Roshko, "The compressible turbulent shear layer: An experimental study," J. Fluid Mech. **197**, 453 (1988).
[26]A. J. Smits and J.-P. Dussauge, *Turbulent Shear Layers in Supersonic Flow* (AIP Press, Melville, NY, 1996).
[27]T. J. O'Hern, "An experimental investigation of turbulent shear flow cavitation," J. Fluid Mech. **215**, 365 (1990).
[28]C. O. Iyer and S. L. Ceccio, "The influence of developed cavitation on the flow of a turbulent shear layer," Phys. Fluids **14**, 3414 (2002).
[29]K. R. Laberteaux and S. L. Ceccio, "Partial cavity flows. Part 1. Cavities forming on models without spanwise variation," J. Fluid Mech. **431**, 1 (2001).
[30]V. Aeschlimann, S. Barre, and S. Legoupil, "X-ray absorption measurements in a cavitating mixing layer for instantaneous 2D void ration determination," Phys. Fluids **23**, 055101 (2011).
[31]M. Dular, R. Bachert, B.Stoffel, and B. Sirok, "Experimental evaluation of numerical simulation of cavitating flow around hydrofoil," Eur J. Mech. B/Fluids **24**, 522 (2005).
[32]M. Dular, R. Bachert, C. Schaad, and B. Stoffel, "Investigation of a re-entrant jet reflection at an inclined cavity closure line," Eur. J. Mech. B/Fluids **26**, 688 (2007).
[33]S. Gopalan and J. Katz, "Flow structure and modeling issues in the closure region of attached cavitation," Phys. Fluids **12**, 895 (2000).
[34]A. Vabre, M. Gmar, D. Lazaro, S. Legoupil, O. Coutier, A. Dazin, W. K. Lee, and K. Fezzaa, "Synchrotron ultra-fast x-ray imaging of a cavitating flow in a Venturi profile," J. Nucl. Instrum. Methods Phys. Res. A **607**, 215 (2009).
[35]J. K. Jakobsen, "On the mechanism of the head breakdown in cavitating inducers," ASME J. Basic Eng. June 1964, 291 (1964).
[36]J. Wu, G. Wang, and W. Shyy, "Time-dependent turbulent cavitating flow computations with interfacial transport and filter-based models," Int. J. Numer. Meth. Fluids **49**, 739 (2005).
[37]R. E. A. Arndt, "Cavitation in vortical flows," Annu. Rev. Fluid Mech. **34**, 145 (2002).
[38]N. Rajaratnam, *Turbulent Jets* (Elsevier Science, Amsterdam, 1976).
[39]J. O. Hinze, *Turbulence*, 1st ed. (McGraw-Hill, Oxford, 1959).
[40]P. E. Dimotakis, "Two dimensional shear-layer entrainment," AIAA J. **24**, 1791 (1986).
[41]H. W. Liepmann and J. Laufer, "Investigations of free turbulent mixing," NACA Technical Note No. 1257, 1947.
[42]I. Wygnansky and H. Fiedler, "The two-dimensional mixing region.," J. Fluid Mech. **41**, 327 (1970).
[43]R. P. Patel, "An experimental study of a plane mixing layer," AIAA J. **11**, 67 (1973).
[44]F. K. Browand and B. O. Latigo, "Growth of the two-dimensional mixing layer from a turbulent and nonturbulent boundary layer. Phys. Fluids **22**, 1011 (1979).
[45]S. Barre, C. Quine and J. P. Dussauge, Compressibility effects on the structure of supersonic mixing layers: Experimental results. J. Fluid Mech. **259**, 47 (1994).
[46]J. L. Lumley and G. Newman, "The return to isotropy of homogeneous turbulence," J. of Fluid Mech. **82**, 161 (1977).
[47]R. Bourguet, M. Braza, G. Harran, and R. El Akoury, "Anisotropic organised eddy simulation for the prediction of non-equilibrium turbulent flows around bodies," J. Fluids Struct. **24**, 1240 (2008).
[48]G. Sridhar and J. Katz, "Effect of entrained bubbles on the structure of vortex rings," J. Fluid Mech. **397**, 171 (1999).